Effects of AlMn dispersoids and Al₃(Sc,Zr) precipitates on the microstructure and ambient/elevated-temperature mechanical properties of hot-rolled AA5083 alloys

Ahmed Y. Algendy [1], Kun Liu [1,*], Paul Rometsch [2], Nick Parson [2], X.-Grant Chen [1,*]

[1] Department of Applied Science, University of Quebec at Chicoutimi, Saguenay (QC), G7H 2B1, Canada

[2] Arvida Research and Development Center, Rio Tinto Aluminum, Saguenay (QC), G7S 4K8, Canada

*Corresponding authors: kun.liu@uqac.ca and xgrant_chen@uqac.ca

Abstract

With the addition of Sc and Zr to AA5083 alloy, two populations of strengthening particles (submicron-sized AlMn dispersoids and nanosized Al₃(Sc,Zr) precipitates) precipitate during three-step heat treatment. Here, their influence on the microstructure and mechanical properties of hot-rolled sheets at ambient and elevated temperatures was investigated. The results show that the low-temperature (25–200 °C) tensile properties of the rolled sheets were significantly improved by increasing the Sc and Zr contents. The yield strength (YS) and ultimate tensile strength (UTS) of the alloy with 0.16 wt.% Sc and 0.17 wt.% Zr at ambient temperature reached 295 and 411 MPa, respectively, showing improvements of 30% in YS and 11.8% in UTS compared to the base alloy. However, the YSs of the Sc/Zr-containing alloys at high temperature (300–400 °C) were lower than that of the base alloy. The mechanical properties of both the base and Sc/Zr-containing alloys were thermally stable during long-term thermal exposure at 300 °C for 500 h, demonstrating the great potential of this alloy for various elevated-temperature applications. The characteristics of the AlMn dispersoids and Al₃(Sc,Zr) precipitates after the heat treatment and hot rolling were examined and quantified using transmission electron microscopy. Their combined contributions toward the YS at 25 and 300 °C were analyzed with the aid of constitutive strengthening equations and compared with experimentally measured values.

Keywords: Aluminum 5083 alloys, Sc and Zr addition, AlMn dispersoids, Al₃(Sc,Zr) precipitates, Mechanical properties, Strengthening mechanism.

1. Introduction

Recently, interest in developing a new generation of lightweight aluminum alloys for automotive and aerospace applications has markedly increased. Owing to their excellent combination of high strength-to-weight ratio, good formability, high toughness, and excellent weldability and corrosion resistance, Al–Mg–Mn 5xxx alloys are considered excellent candidates for transportation (automotive, shipbuilding, etc.) and structural components, as well as many other applications [1, 2]. Traditionally, 5xxx aluminum alloys are classified as non-heat-treatable

alloys, and their strength can only be achieved by strain hardening and solid-solution strengthening [3, 4]. Therefore, the achievable strength of this alloy series is more limited than that of heat-treatable high-strength aluminum alloys, thus restricting their performance in several applications.

In addition to strain hardening, dispersoid strengthening has recently been identified as a promising approach for improving the mechanical strength of non-heat-treatable aluminum alloys, such as 3xxx alloys [5-8]. Several studies have reported that appropriate heat treatments can promote the precipitation of fine and densely distributed dispersoids, thereby enhancing the ambient- and elevated-temperature mechanical properties [6-9]. A recent study on Al–Mg–Mn 5xxx alloys [10] demonstrated that a multistep heat treatment can be used to precipitate high volume fractions of submicron-sized AlMn dispersoids and improve the rolling performance and mechanical properties of rolled sheets.

In recent years, Sc, as an effective microalloying element, has often been added to aluminum alloys to enhance their mechanical properties by forming nanosized $L1_2$-Al_3Sc precipitates during aging treatment in the temperature range of 300–425 °C [11-14]. These finely dispersed $L1_2$-Al_3Sc precipitates are fully coherent with the aluminum matrix and exhibit high thermal stability at elevated temperatures (300–350 °C) owing to the low diffusivity of Sc in Al [15, 16]. For industrial applications, cost-effective Zr is often added along with Sc. Zr can substitute with Sc to form core–shell $L1_2$-$Al_3(Sc,Zr)$ precipitates that have better coarsening resistance than Al_3Sc precipitates, thereby improving the recrystallization resistance and elevated-temperature properties [17-20].

In several studies, Sc and Zr have been coadded to improve the mechanical properties of traditional heat-treatable alloys, such as 2xxx, 6xxx, and 7xxx alloys [21-23]. Significant improvements in the room-temperature microhardness and mechanical properties have been reported, mainly owing to the combined strengthening effect of aging strengthening phases (Al_2Cu, Mg_2Si, and $MgZn_2$) and $Al_3(Sc,Zr)$ precipitates. For instance, the coaddition of Sc and Zr increases the tensile strength and high-cycle fatigue strength of AA6106 alloys [21], and noticeably increases the hardness of AA2219 alloys [22]. However, owing to the high coarsening rate of the strengthening phases (Al_2Cu, Mg_2Si, and $MgZn_2$) of heat-treatable alloys at elevated temperatures, most studies on Sc and Sc+Zr additions have focused on the ambient-temperature properties [24, 25], creep behavior of cast alloys [11, 19], or superplastic deformation of processed alloys [26, 27]. In addition, the temperatures for precipitating conventional aging strengthening phases (Al_2Cu, Mg_2Si, and $MgZn_2$) are very different from those for $Al_3(Sc,Zr)$ precipitates, making the heat treatment of both types of phase incompatible. Therefore, the benefits of microalloying with Sc and Zr and the precipitation of fine and thermally stable $Al_3(Sc,Zr)$ precipitates cannot be fully applied.

In Al–Mg–Mn alloys, the precipitation temperatures of AlMn dispersoids and $Al_3(Sc,Zr)$ precipitates are similar, and both phases are thermally stable and coarsening-resistant, which provides a common basis for improving the ambient- and elevated-temperature properties during

heat treatment. However, there is little information on the synergetic effects of these strengthening phases on the elevated-temperature mechanical properties of Al–Mg–Mn 5xxx alloys.

The main objective of this study was to explore the combined effects of two populations of strengthening particles (submicron-sized AlMn dispersoids and nanosized $Al_3(Sc,Zr)$ precipitates) on the mechanical properties of Al–Mg–Mn AA5083 alloys. To clarify the roles of microalloyed Sc and Zr, the microstructural evolution after heat treatment and hot rolling was characterized by several techniques, including optical microscopy, scanning electron microscopy (SEM), and transmission electron microscopy (TEM). The tensile properties of hot-rolled sheets were evaluated at ambient and elevated temperatures. Finally, the experimentally measured yield strengths (YSs) were compared with the analytically calculated ones using constitutive strengthening equations to better understand the strengthening mechanisms of Sc/Zr-containing AA5083 alloys.

2. Experimental procedure

Three Al–Mg–Mn alloys were prepared from commercially pure Al (99.7%) and Mg (99.8%), as well as Al–25% Fe, Al–50% Si, Al–25% Mn, Al–20% Cr, Al–50% Cu, Al–2% Sc, and Al–15% Zr master alloys (all the alloy compositions used in this study were in wt.%). The alloys were denoted as base alloy B (AA5083, Sc/Zr-free), B08 (0.08% Sc and 0.08% Zr), and B15 (0.16% Sc and 0.17% Zr). The materials were melted in a graphite crucible in an electrical resistance furnace. The melting temperature was maintained at 780 °C for 30 min followed by degassing with pure Ar for 15 min. Al–5% Ti–1% B master alloy was added as a grain refiner. Then, the melt was poured into a permanent steel mold preheated at 250 °C to produce cast ingots with dimensions of $30 \times 40 \times 80$ mm. The chemical compositions were analyzed using optical emission spectrometry, and the results are listed in Table 1.

Table 1 Chemical composition of experimental alloys

Alloys	Elements, wt.%								
	Mg	Mn	Si	Fe	Cu	Cr	Ti	Sc	Zr
B (base)	4.78	0.79	0.26	0.31	0.12	0.14	0.09	---	---
B08	4.76	0.79	0.26	0.35	0.10	0.15	0.10	**0.08**	**0.08**
B15	4.75	0.81	0.31	0.31	0.11	0.15	0.09	**0.16**	**0.17**

To promote the precipitation of AlMn dispersoids and $Al_3(Sc,Zr)$ precipitates [10, 28], the cast ingots were heat-treated using a three-step heat treatment (275 °C/12 h + 375 °C/48 h + 425 °C/12 h) followed by water quenching to room temperature. Subsequently, the heat-treated ingots were machined to 25 mm thick and then hot rolled to a final sheet thickness of 3.2 mm (87% reduction

in thickness) using a laboratory-scale rolling mill. Multiple hot-rolling passes were carried out at a temperature of 500 ± 10 °C. Before mechanical tests, all rolled sheets were annealed at 300 °C for 5 h to relieve the residual stress generated during rolling.

The tensile properties at room temperature were measured using Instron 8801 servo-hydraulic testing unit at strain rate 0.5 mm/min. The tensile samples were machined according to ASTM E8/E8M-16a in the rolling direction with a gauge size of 3 x 6 mm. The tensile properties at 300 °C were measured on a Gleeble 3800 thermomechanical testing unit at a strain rate of 0.001 s^{-1}, in which the tensile samples were heated to 300 °C with a heating rate of 2 °C/sec and then holding 180 s prior to tensile loading. Average results were reported from three tests in a given condition.

Samples for microstructural observations were prepared using a standard metallographic procedure. The grain structure was observed using an optical microscope (Nikon, Eclipse ME600) under polarized light after electro-etching with Barker's agent (3 vol.% HBF$_4$ solution) at 15 V for 3 min. After heat treatment or rolling, the samples were etched in 0.5% HF for 30 s to reveal the general distribution of AlMn dispersoids. The grain and subgrain structures after rolling were characterized using electron backscatter diffraction (EBSD). The EBSD samples were sectioned from the gauge of the tensile samples, parallel to the rolling and tensile deformation directions. A transmission electron microscope (JEM-2100) operated at 200 kV was used to observe the distribution of AlMn dispersoids and Al$_3$(Sc,Zr) precipitates in detail. All TEM images were obtained along the [001]$_{Al}$ zone axis to observe the AlMn dispersoids To clearly reveal the Al$_3$(Sc,Zr) precipitates, centered superlattice dark-field images were recorded along the [100] reflections close to the <011> direction. The characteristics of the AlMn dispersoids and Al$_3$(Sc,Zr) precipitates were quantified from the TEM images using ImageJ image analysis software. The number density N_d and volume fraction V_f of AlMn dispersoids were determined using the following equations [7, 11]:

$$N_d = \frac{N}{A(D + t)} \qquad (1)$$

$$V_f = A_A \frac{K\overline{D}}{K\overline{D} + t}(1 - A_{DFZ}) \qquad (2)$$

Where N is the number of particles; A and $\overline{D}$ are the total area and the equivalent diameter of the particles, respectively; t is the thickness of the TEM foil; A$_A$ is the area fraction of dispersoids in the TEM image; K is the average shape factor of dispersoids equal to 0.45 [9]; A$_{DFZ}$ is the area fraction of DFZ measured in the optical images.

3. Results

3.1 As-cast and heat-treated microstructures

Fig. 1 shows the grain structure and distribution of intermetallic phases in the as-cast alloys. All three alloys had equiaxed grain structures (Fig. 1a and b). The average grain size of alloy B

was 64.8 μm, whereas those of alloys B08 and B15 were 60.8 and 54 μm, respectively. This reduction in grain size results from the grain-refining effect of the Sc+Zr addition [24, 29, 30]. As shown in Fig. 1c and d, the as-cast alloys contained α-Al dendritic cells with several intermetallic phases distributed at the dendrite boundaries. The dominant intermetallic compounds (IMC) in all three alloys were Fe/Mn-rich α-Al_{15}(Fe,Mn,Cr)$_3$Si$_2$ and Al_6(Fe,Mn,Cr) intermetallics and primary Mg_2Si intermetallics (dark color), as identified by SEM–energy dispersive X-ray spectroscopy (SEM-EDS) analysis. A small amount of low-melting-point τ-Al_6CuMg_4 eutectic phase was also detected in the interdendritic regions. Interestingly, the amount of intermetallic phases increased significantly with the addition of Sc and Zr. The results of image analysis confirmed that the area fraction of Fe/Mn-rich intermetallics (α-Al_{15}(Fe,Mn,Cr)$_3$Si$_2$ and Al_6(Fe,Mn,Cr)) increased from 1.98% in alloy B to 2.31% in alloy B08 and further to 3.14% in alloy B15, while the area fraction of primary Mg_2Si intermetallics increased from 0.7% in alloy B to 0.77% in alloy B08 and further to 0.9% in alloy B15. This could be attributed to the decreased solubility of Mn and Mg owing to the addition of Sc and Zr [11, 31].
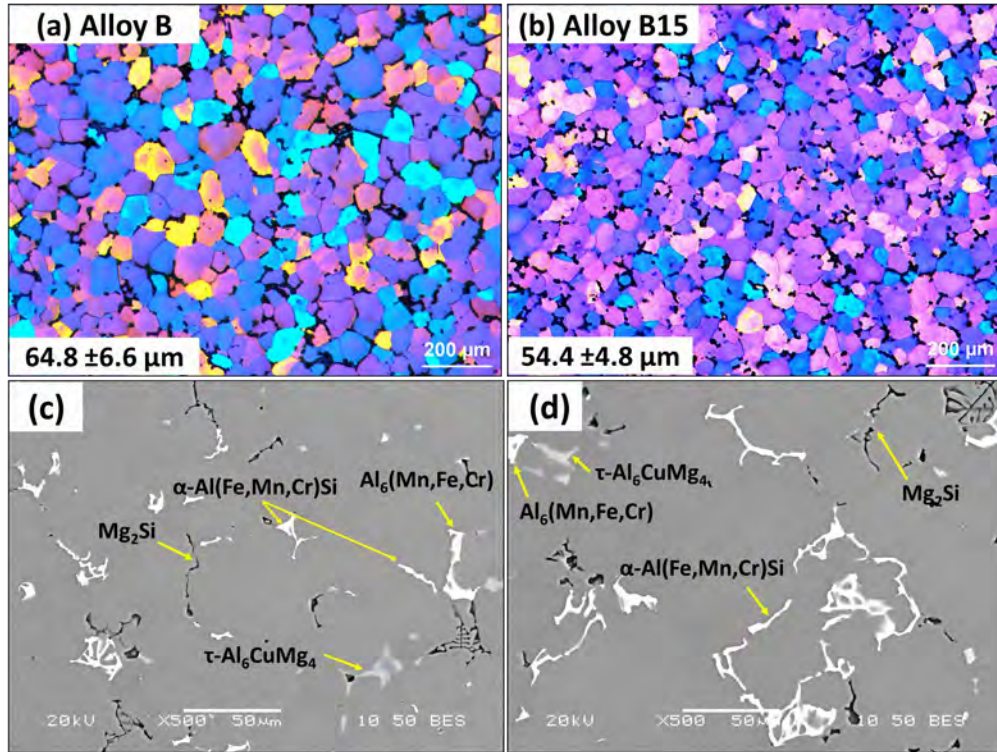

Figure 1: Optical images showing the grain structures of (a) alloy B and (b) alloy B15, and SEM backscattered images showing the distribution of intermetallic phases of (c) alloy B and (d) alloy B15 in the as-cast condition.

Fig. 2 shows the typical microstructures of the three alloys after the three-step heat treatment. As shown in the optical images (Fig. 2a-c), a large number of dispersoids formed in the dendritic cells during heat treatment, appearing as dispersoid zones (DZ, dark areas marked with red lines). In addition, dispersoid-free zones (DFZ, light area marked with blue lines) were observed in the interdendritic regions surrounding the intermetallic phases. It should be noted that complete

dissolution of the low-melting-point τ-Al$_6$CuMg$_4$ eutectic phase and partial dissolution of the primary Mg$_2$Si intermetallics occurred during the heat treatment. Bright-field TEM images (Fig. 2d-f) revealed the precipitation of submicron-sized AlMn dispersoids with cube- and rod-like morphologies in the DZs. The AlMn dispersoids were identified as Al$_4$Mn and Al$_6$Mn by TEM-EDS and selected area diffraction patterns [10]. The equivalent diameter of the AlMn dispersoids in base alloy B was ~25 nm, and the number density was ~560 µm^{-3}. However, with increasing Sc and Zr contents in alloys B08 and B15, the size of the dispersoids increased and the number density decreased compared to that in alloy B (Fig. 2g).
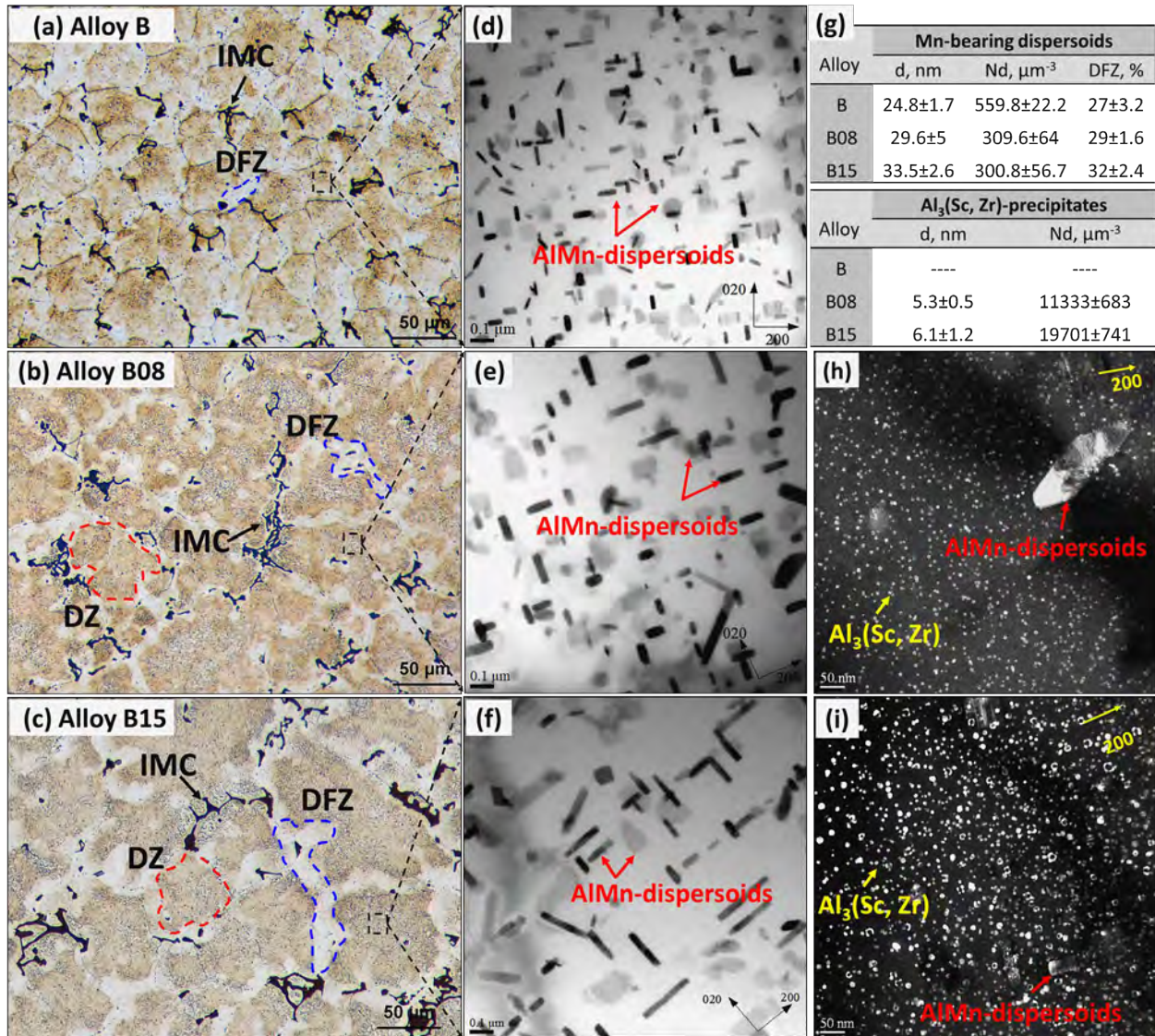

Figure 2: Typical microstructures after heat-treatment: (a, b, c) optical images and (d, e, f) bright-field TEM images showing the distribution of AlMn dispersoids for alloys B, B08 and B15, respectively; (h, i) dark-field TEM images showing the distribution of Al$_3$(Sc,Zr) precipitates for alloys B08 and B15; (g) characteristics of two population of particles (AlMn dispersoids and Al$_3$(Sc,Zr) precipitates).

In addition to the AlMn dispersoids, a large number of nanosized Al$_3$(Sc,Zr) precipitates were formed in alloys B08 and B15, as shown in the dark-field TEM images (Fig. 2h and i). The Al$_3$(Sc,Zr) precipitates were uniformly distributed in the Al matrix and were much finer and denser than the AlMn dispersoids. A summary of the two populations of particles is shown in Fig. 2g. This figure shows that the addition of Sc and Zr caused the following microstructural changes: 1) a high number of nanosized Al$_3$(Sc,Zr) precipitates coexisted with AlMn dispersoids, 2) the size of the AlMn dispersoids increased and the number density (Nd) of dispersoids decreased, and 3) the area fraction of DFZs increased.

There are two possible reasons for the increased size and decreased number density of dispersoids in alloys B8 and B15. First, the addition of Sc and Zr lowers the solubility of Mn, Mg, and Si in the aluminum matrix [11, 15, 31-34]. Therefore, the addition of Sc and Zr would promote the formation of Fe/Mn-rich intermetallics, thereby increasing their volume fraction. Consequently, the amount of supersaturated Mn in the α-Al solid solution would be reduced, leaving less Mn available for the formation of AlMn dispersoids upon heat treatment. The other reason is that the addition of Sc and Zr decreases the nucleation efficiency of AlMn dispersoids during heat treatment. As reported previously [10, 35-37], metastable β′-Mg$_2$Si phases may act as nucleation sites for the precipitation of AlMn dispersoids. Owing to the reduced solubility of Mg and Si, more Mg and Si would be consumed to form primary Mg$_2$Si particles during solidification, lowering their supersaturation levels in the α-Al matrix. Therefore, during the heating process and first step of the heat treatment (i.e., 275 °C/12 h), a lower number of β′-Mg$_2$Si particles would form in the Sc/Zr-containing alloys than in the base alloy, resulting in a lower number density of AlMn dispersoids being precipitated in the subsequent heat treatment step.

3.2 Microstructures after hot rolling

After heat treatment, all three alloys were hot rolled at 500 °C. The typical microstructures after hot rolling are illustrated in Fig. 3. Owing to the high deformation ratio (87% reduction), the intermetallic particles were fragmented and aligned in the rolling direction, and the grains were also elongated in the rolling direction, as shown in Fig. 3a-c. Bright-field TEM images (Fig. 3d-f) revealed that the AlMn dispersoids coarsened during hot rolling; compared to the heat-treated alloys, the size of the dispersoids was increased, and their number density was remarkably decreased (Fig. 2). The quantitative results in Table 2 show that the number density of AlMn dispersoids decreased after hot rolling by 59%, 80%, and 79% for alloys B, B08, and B15, respectively. Base alloy B still exhibited the highest number density of dispersoids among the three alloys.

A similar coarsening trend was observed for the Al$_3$(Sc,Zr) precipitates in alloys B08 and B15 after hot rolling, as shown in Fig. 3g and h. The fine and spherical Al$_3$(Sc,Zr) particles became larger and less dense than those in the heat-treated samples. For instance, the number density sharply dropped from 11,333 to 2718 μm^{-3} in alloy B08 and from 19,701 to 5695 μm^{-3} in alloy

B15 (Fig. 2 and Table 2), representing reductions of 76% and 71%, respectively. The lower density and larger size of the Mn-bearing dispersoids and $Al_3(Sc,Zr)$ precipitates are predominantly attributed to the high rolling temperature (500 °C), at which both AlMn dispersoids and $Al_3(Sc,Zr)$ precipitates are no longer thermally stable [7, 14-17, 38]. In addition, the high number density of dislocations generated during rolling accelerates the diffusion of alloying elements in the matrix, resulting in the growth and coarsening of both types of particle [39-41].
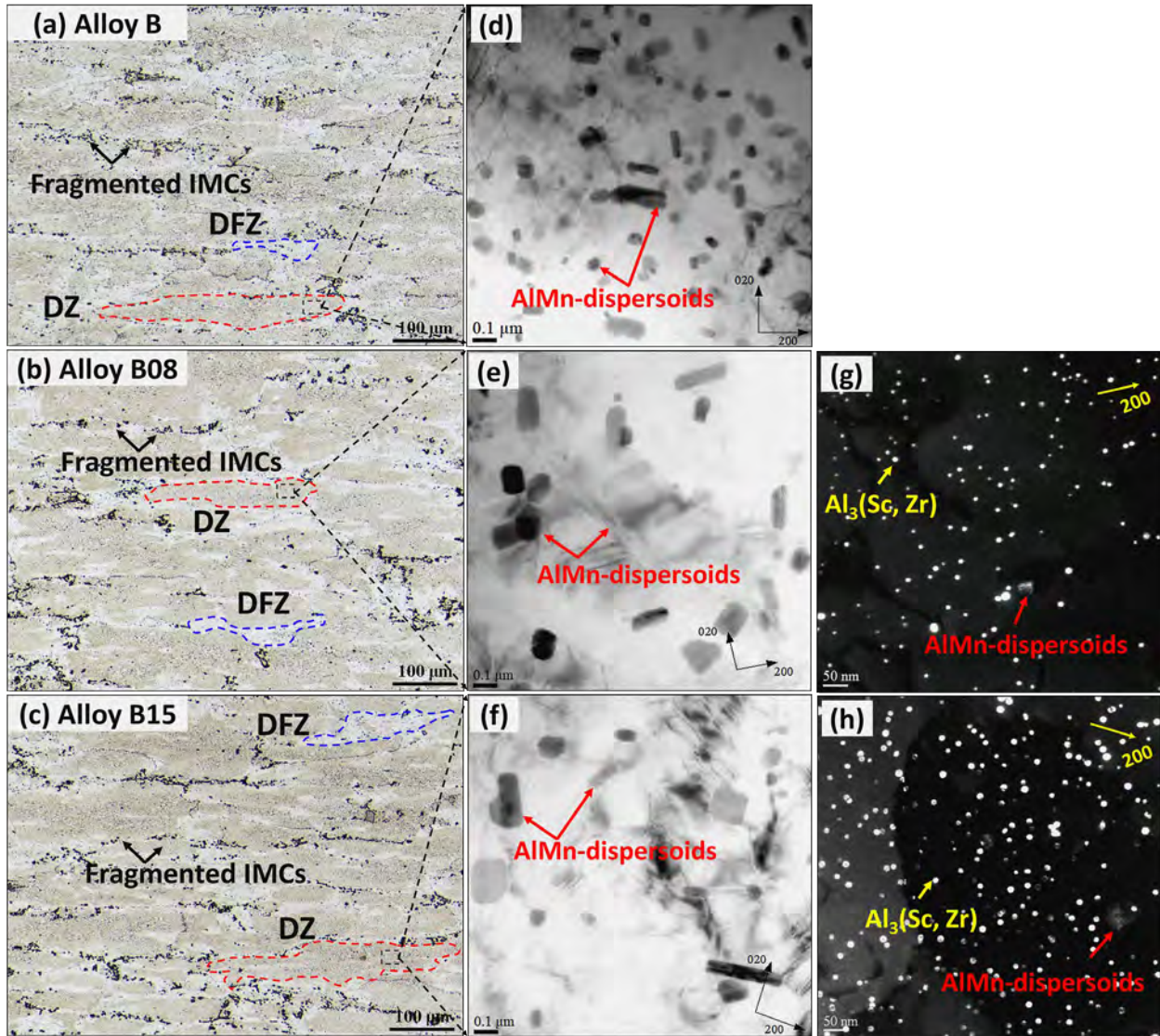

Figure 3: Typical microstructures of the hot-rolled samples: (a, b, c) OM images and (d, e, f) bright-field TEM images showing the distribution of AlMn dispersoids for alloys B, B08 and B15, respectively; (g, h) dark-field TEM images showing the distribution of $Al_3(Sc,Zr)$ precipitates for alloys B08 and B15.

8

Table 2: Quantitative TEM results of AlMn dispersoids and Al₃(Sc,Zr) precipitates after rolling.

Alloy	AlMn dispersoids			Al₃(Sc,Zr) precipitates		
	d (nm)	N_d (µm⁻³)	V_f (%)	d (nm)	N_d (µm⁻³)	V_f (%)
B	32.4±0.2	231±46	1.4	--	--	--
B08	57.2±0.6	60.1±9.6	1.02	11.9±0.5	2718±385	0.19
B15	56.0±0.6	64.8±13.3	1.06	12.6±0.4	5695±297	0.49

3.3 Mechanical properties of hot-rolled sheets at ambient and elevated temperatures

Fig. 4 shows the ambient-temperature tensile properties of all three hot-rolled alloys. The addition of Sc and Zr significantly improved the alloy strength, while the elongation decreased. Fig. 4a displays typical engineering stress–strain curves; after reaching the peak stress (ultimate tensile strength (UTS)), the curve underwent a short plateau followed by an instantaneous drop. As shown in Fig. 4b, the tensile strength increased with increasing Sc content, and alloy B15 exhibited the highest YS and UTS at 295 and 411 MPa, respectively. These values are 30% and 11.8% higher, respectively, than those for base alloy B. On the other hand, in low-Sc alloy B08, the YS and UTS were 262 and 392 MPa, respectively, representing an improvement of 14% and 3%, respectively, relative to those of base alloy B. The increase in tensile strength via the addition of Sc and Zr was mainly due to the introduction of fine and coherent Al₃(Sc,Zr) precipitates as an additional strengthening phase (Fig. 3).
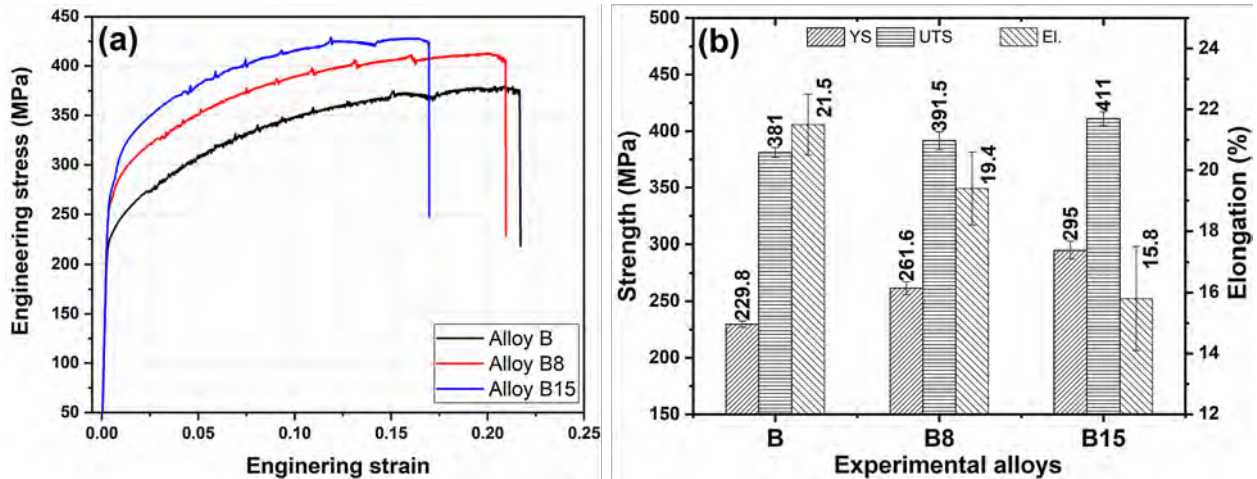

Figure 4: (a) Typical engineering stress-strain curves of experimental alloys and (b) tensile properties at ambient temperature for three hot-rolled alloys.

The elevated-temperature tensile properties of the hot-rolled alloys are shown in Fig. 5. Fig. 5a shows the engineering stress–strain curves measured at 300 °C. Shortly after tensile loading, the curves of all alloys quickly rose to the maximum stress (UTS) and then gradually decreased until reaching a strain of 0.6–0.7. It is apparent that the elevated-temperature ductility of the alloys is no longer a concern because the elongation of all three alloys exceeded 60%. As shown in Fig. 5b, the UTS of both Sc/Zr-containing alloys (99 MPa) was only slightly lower than that of the base alloy (104 MPa). However, the YSs of both B08 and B15 alloys (66 MPa) were significantly lower than that of alloy B (88 MPa). This is equivalent to a 24% reduction in YS compared to that of the Sc-free base alloy. Notably, this trend is completely different from that at ambient temperature. In addition, although alloy B15 contained more $Al_3(Sc,Zr)$ precipitates (Table 2), the YS and UTS of alloys B08 and B15 were almost the same.
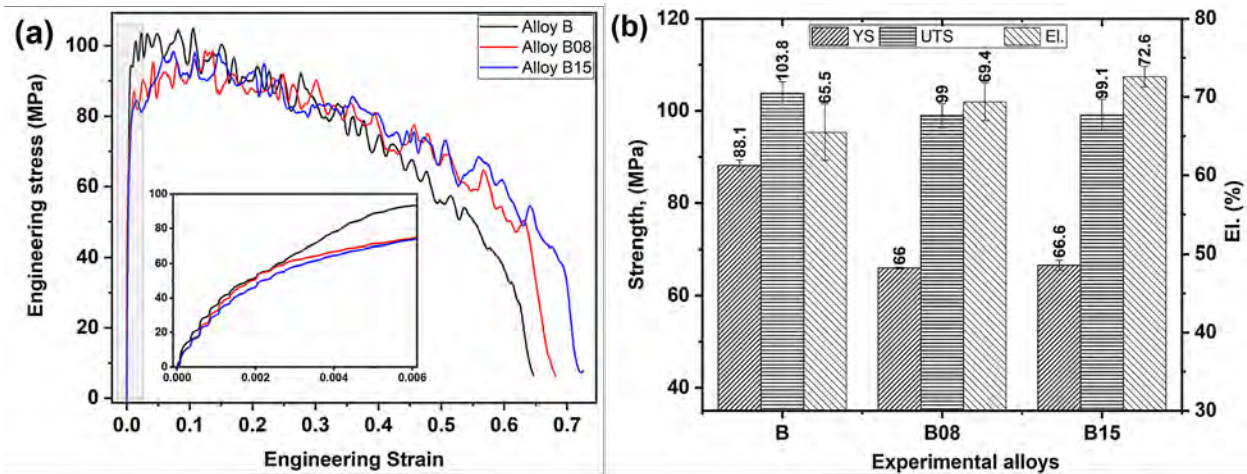

Figure 5: (a) Typical engineering stress-strain curve of experimental alloys and (b) tensile properties at 300 °C.

To better understand the effect of temperature on the tensile properties, all three hot-rolled alloys were subjected to tensile tests at temperatures of 25–400 °C, and the tensile properties are presented in Fig. 6. As expected, the tensile strengths decreased gradually with increasing test temperature for all three alloys. At 25–200 °C, the Sc/Zr-containing alloys (B08 and B15) exhibited higher tensile strengths (both YS and UTS) than base alloy B, and the YS and UTS increased with increasing Sc content. At 250 °C, alloys B and B08 had similar YS (150 vs. 147.2 MPa), but alloy B15 showed noticeably lower YS of 123.2 MPa (Fig. 6a). As the testing temperature increased to 300–400 °C, although the YS of the Sc/Zr-containing alloys (B08 and B15) remained equal, the YS became considerably lower than that of base alloy B. For instance, at 400 °C, both alloys B08 and B15 had a YS of 21 MPa, which was lower than that of base alloy B (32 MPa). The UTS showed a slightly different trend from that of the YS (Fig. 6b). At relatively low temperatures (25–200 °C), the UTSs of the Sc/Zr-containing alloys were higher than that of alloy B. However, at 250 °C, the UTSs of all three alloys were almost the same. At higher temperatures (300–400 °C), the UTSs of all three alloys were still very close.
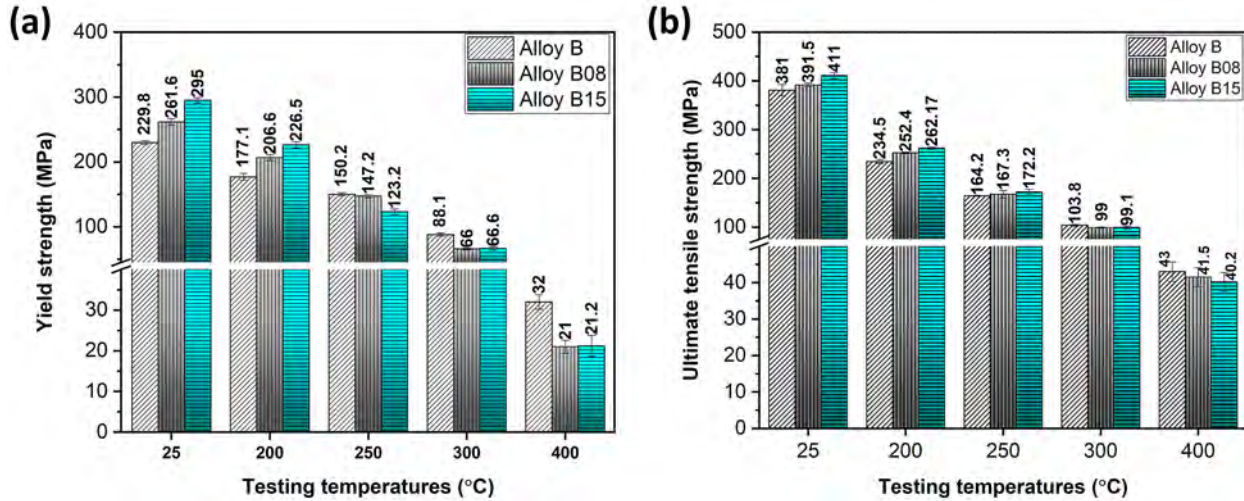
Figure 6: (a) YS and (b) UTS of experimental alloys as a function of testing temperatures.

The thermal stability of the mechanical properties is an important consideration for aluminum alloys that can potentially be used at elevated temperatures. Therefore, the thermal stability of two of the hot-rolled alloys (B and B15) was evaluated by exposing them at 300 °C for up to 500 h. The tensile strengths at 25 and 300 °C as a function of the exposure time are displayed in Fig. 7. Both the YS and UTS remained unchanged after long-term thermal exposure of up to 500 h for both alloys. For instance, the YSs at 25 °C remained at 230 MPa for alloy B and 295 MPa for alloy B15, while the elevated-temperature YSs were stable at 85 MPa (alloy B) and 68 MPa (alloy B15) throughout the entire long-term thermal exposure. These results confirm the excellent thermal stability and low coarsening kinetics of AlMn dispersoids and $Al_3(Sc,Zr)$ precipitates at 300 °C for Al-Mg-Mn alloys strengthened by both types of particles.
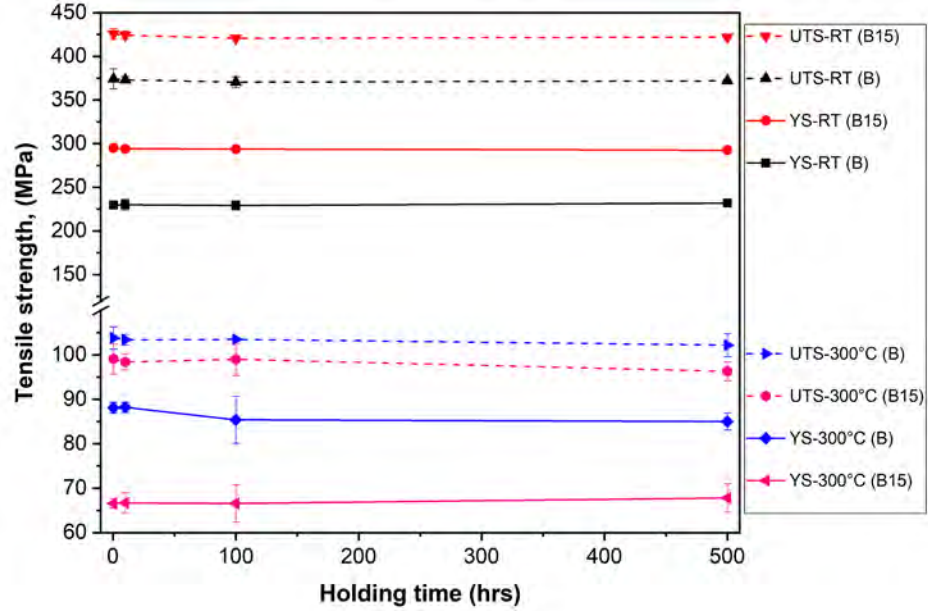
Figure 7: Evolution of YS and UTS of alloys B and B15 tested at 25 °C and 300 °C as a function of the time of thermal exposure at 300 °C.

4. Discussion

4.1 Constitutive analysis of yield strength at ambient and elevated temperatures

The overall mechanical strength of aluminum alloys is determined by the stress required to overcome various obstacles during deformation. Several strengthening mechanisms are operative, including solid-solution strengthening, grain-boundary strengthening, and particle strengthening. To better understand the strengthening effect of the two distinct groups of particles (AlMn dispersoids and Al₃(Sc,Zr) precipitates) at ambient and elevated temperatures, the YSs of the experimental Al–Mg–Mn alloys were quantitatively studied using constitutive equations. Assuming that the contributions of the strengthening mechanisms are independent and can be linearly added, the overall YS can be expressed as follows:

$$\Delta\sigma_{YS} = \sigma_o + \Delta\sigma_{SS} + \Delta\sigma_{GB} + \Delta\sigma_{dispersoids} + \Delta\sigma_{precipitates} \qquad (3)$$

where $\Delta\sigma_{YS}$ is the overall yield strength, σ_o is the strength of the pure Al matrix, and $\Delta\sigma_{SS}$, $\Delta\sigma_{GB}$, $\Delta\sigma_{dispersoids}$, and $\Delta\sigma_{precipitates}$ are the strengthening contributions of solid-solution strengthening, grain-boundary strengthening, the AlMn dispersoids, and the Al₃(Sc,Zr) precipitates.

4.1.1 Strengthening mechanisms at ambient temperature

The yield strength of the Al matrix was considered to be 34 MPa, as taken from an annealed pure 1100-O Al alloy [11]. The solid-solution strengthening of AA5083 alloys is mainly attributed to Mg and Mn; the other elements have a negligible contribution owing to their small contents. Mg is primarily consumed by primary Mg_2Si and the low-melting-point τ-Al_6CuMg_4 eutectic phase. After heat treatment and hot rolling, the τ-Al_6CuMg_4 eutectic phase was entirely dissolved, and Mg_2Si was mostly dissolved. By measuring the remaining volume fraction of Mg_2Si, the availability of Mg solutes in the solid solution was estimated. The consumption of Mn is strongly related to the formation of Fe/Mn-rich intermetallics and AlMn dispersoids. Therefore, the Mn concentration in the aluminum matrix can be assessed based on their volume fractions after hot rolling. The strengthening contributions of Mg and Mn were calculated using Eq. 4 [3, 4].

$$\Delta\sigma_{ss} = KC^n \tag{4}$$

where C is the concentration of solute atoms (wt.%), $K_{Mg} = 13.8$ MPa/wt.%, $n_{Mg} = 1.14$, $K_{Mn} = 18.35$ MPa/wt.%, and $n_{Mn} = 0.9$ [3]. The calculation showed that the strengthening effects caused by Mg and Mn solutes were 77 and 3.5 MPa, respectively (Table 3).

The contribution of grain boundary strengthening to the YS was predicted using the Hall–Petch equation [3]:

$$\sigma_{GB} = K_y/(d_{GB})^{0.5} \tag{5}$$

where K_y is the Hall–Petch constant, which is typically considered to be 0.22 MPa/m$^{0.5}$ for Al–4 wt.% Mg alloys [3], and d_{GB} is the average grain size of the hot-rolled samples. The measured average grain sizes of alloys B, B8, and B15 were 64.8, 64.2, and 59.4 μm, respectively.

For the precipitation strengthening mechanism, the contribution of the two types of particles (AlMn dispersoids and $Al_3(Sc,Zr)$ precipitates) to the ambient-temperature YS can be explained and predicted using the classical Orowan bypass mechanism because of their relatively large size [19]. Therefore, the contributions of both types of strengthening particle were calculated using Eqs. 6 and 7 [11, 19, 42, 43].

$$\Delta\sigma_{dispersions} = \frac{0.84MGb}{2\pi(1-v)^{0.5}\lambda}\ln\left(\frac{r}{b}\right) \tag{6}$$

$$\lambda = r\left(\frac{2\pi}{3V_f}\right)^{0.5} \tag{7}$$

where M (= 3) is the Taylor factor, G (= 27.4 GPa) is the shear modulus of the Al matrix, b (= 0.286 nm) is the Burgers vector, v (= 0.33) is Poisson's ratio, λ is the effective interparticle spacing,

r is the equivalent average radius of the dispersoids/precipitates, and V_f is the volume fraction of particles [19, 42, 43].

Using the data in Table 2 and Eqs. 6 and 7, the increments in YS due to the presence of AlMn dispersoids and Al$_3$(Sc,Zr) precipitates were computed (Table 4). AlMn dispersoids provided an increment of 80.1 MPa to the YS of the base alloy B. However, with the addition of Sc and Zr, the YS increment due to AlMn dispersoids decreased by a factor of two because the addition of Sc and Zr significantly decreased the number density and volume fraction of dispersoids (Fig. 3, Table 2). The increments in YS due to the presence of fine and dense Al$_3$(Sc,Zr) precipitates were calculated to be 59.3 MPa in alloy B08 and 89.8 MPa in alloy B15. The decrease in YS increment from the AlMn dispersoids in the two Sc/Zr-containing alloys was compensated by Al$_3$(Sc,Zr) precipitates. Owing to the coexistence of the two types of particles, the contribution of particle strengthening is higher in alloys B08 and B15 than that in the base alloy.

As shown in Table 3, in the case of the Sc-free base alloy, the highest contribution to the YS is from AlMn dispersoids (80 MPa), followed by the Mg solid solution (77 MPa). In the two Sc/Zr-containing alloys, B08 and B15, precipitation strengthening due to the coexisting AlMn dispersoids and Al$_3$(Sc,Zr) precipitates provided the largest contribution in strength, with the strengthening contribution of the Al$_3$(Sc,Zr) precipitates exceeding that of the AlMn dispersoids.

Fig. 8a shows a comparison of the predicted and experimentally measured YSs for all three alloys. Although the predicted YSs were slightly lower than the measured ones, the general trend agreed well between the predicted and experimental results. Consequently, the constitutive equation is suitable for predicting the YS of deformed samples containing different types of precipitates.

Table 3: Predicted YS contributions and experimentally measured YS at 25 ºC (MPa)

Alloy	B	B8	B15
Al matrix (1100-O)	34	34	34
Mg solid solution	76.8	75.7	74.4
Mn solid solution	3.5	3.5	2.3
Grain boundary	27.3	27.4	28.5
AlMn dispersoids	80.1	43.2	44.7
Al$_3$(Sc,Zr) precipitates	---	59.3	89.8
Predicted YS	221.7	243.1	273.9
Experimental results	229.8	261.6	295

4.1.2 Strengthening mechanisms at elevated temperature (300 ºC)

Owing to a lack of high-temperature data and appropriate constitutive equations, the elevated-temperature strengthening mechanisms are less well-understood than those at ambient temperature. A few studies have used different approaches to predict the elevated-temperature strength [11, 19, 44]. It is difficult to estimate the contributions of solid-solution and grain-boundary strengthening at elevated temperatures using Eqs. 4 and 5. To simplify the case and focus on the main factor (i.e., precipitation strengthening), the available YS data for AA5083-O at 315 °C (52 MPa) [45] was used as a close approximation for the matrix, solid solution, and grain boundary contributions at 300 °C.

The elastic interaction between dislocations and coherent precipitates causes repulsive stress that hinders dislocation motion [44, 46]. However, at high temperatures, the induced thermal energy allows dislocations to overcome this repulsive stress by enabling dislocation climb. Owing to their size range, the dislocation climb mechanism was considered to better estimate the strength contribution of the nanosized $Al_3(Sc,Zr)$ precipitates [11, 44]. The strength increment caused by dislocation climb strengthening ($\Delta\sigma_{Climb}$) is the sum of the modulus and lattice mismatch strength increments ($\Delta\sigma_{MMC}$ nad $\Delta\sigma_{LMC}$) according to Eqs. 8 and 9 [44, 46].

$$\Delta\sigma_{Climb\ (Al3(Sc,Zr))} = \Delta\sigma_{MMC} + \Delta\sigma_{LMC} \tag{8}$$

$$\Delta\sigma_{Climb} = 0.0055M'\Delta G^{1.5}\left(\frac{2V_f}{G_m}\right)^{0.5}\left(\frac{r}{b}\right)^{\frac{3m}{2}-1} + \chi M'(\varepsilon)^{1.5}G_m\left(\frac{2V_f r}{b}\right)^{0.5} \tag{9}$$

where M' (= 3.06) is the mean matrix orientation factor; G_m (= 21.1 GPa) is the shear modulus of the Al matrix at 300 °C; ΔG (= $G_p - G_m$) is the difference in modulus between the matrix and precipitates, where G_p (= 66.2 GPa) is the shear modulus of the precipitates; b (= 0.288 nm) is the Burgers vector; υ (= 0.33) is Poisson's ratio; χ (= 2.6) and m (= 0.85) are constants; ε is the contrained strain); r is the equivalent average radius of the particles; and V_f is the volume fraction of the particles [44, 46].

Because the size of AlMn dispersoids is relatively large, their predominant strengthening mechanism is Orowan bypass strengthening [44]. Thus, the YS contribution of the AlMn dispersoids at elevated temperatures can still be estimated using Eqs. 6 and 7, considering only the change in the shear modulus of the matrix, G_m, from 27.4 GPa (25 °C) to 21.1 GPa (300 °C).

Table 4 displays the calculated YS increments of the AlMn dispersoids and $Al_3(Sc,Zr)$ precipitates, and Fig. 8b shows a comparison of the predicted and experimental YS values at 300 °C. Compared to their contribution at room temperature, the strengthening increments of the AlMn

dispersoids and Al₃(Sc,Zr) precipitates decreased by a factor of two at 300 °C for all three alloys. This was attributed to the change in the shear modulus (G_m) and the sufficient thermal energy at elevated temperatures. In the Sc/Zr-containing alloys, B08 and B15, it was predicted that the total contribution of the coexisting AlMn dispersoids and Al₃(Sc,Zr) precipitates was higher than the contribution of AlMn dispersoids to base alloy B. However, the experimentally measured YSs exhibited the opposite trend; that is, the measured YSs of B08 and B15 were considerably lower than that of base alloy B. The reasons for this are explored in the following section.

Table 4: Predicted YS contributions and experimentally measured YS at 300 °C (MPa)

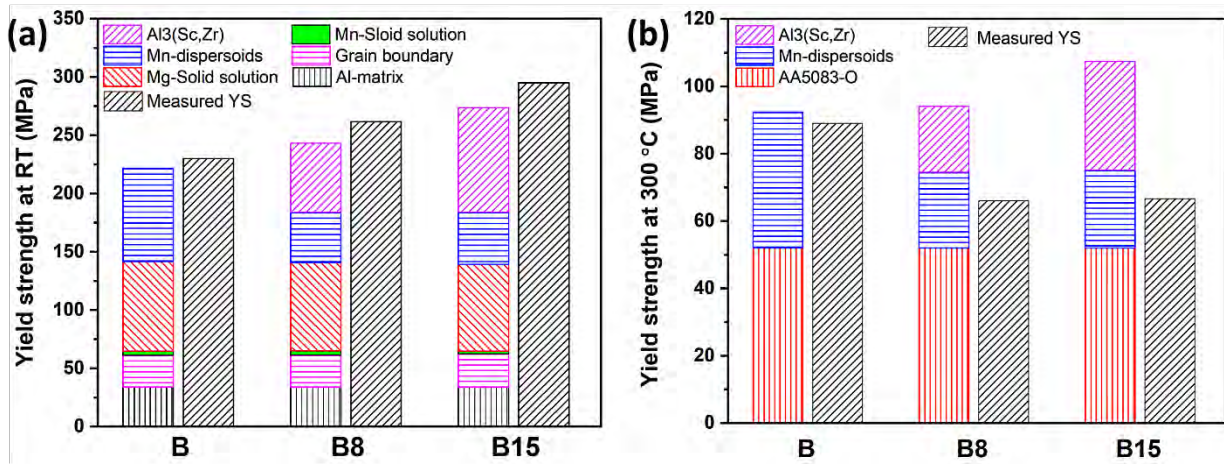| Alloy	B	B08	B15
AA 5083-O	52	52	52
AlMn dispersoids	40.3	22.5	23.1
Al₃(Sc,Zr) precipitates	---	19.6	32.3
Predicted YS	92.3	94.1	107.4
Experimental results	88	66	67

Figure 8: Comparison between predicted and experimental yield strengths for three alloys, (a) at ambient temperature and (b) at 300 °C.

4.2 Other factor influencing the elevated-temperature yield strength

As shown in Fig. 8a, the predicted ambient-temperature YSs agreed well with the experimental results. However, there was a large discrepancy between the predicted and experimental YSs at

300 °C for both Sc/Zr-containing alloys (B08 and B15) (Fig. 8b). In fact, the Sc/Zr-containing alloys had considerably lower YSs at 300 °C than the Sc-free base alloy (Fig. 5b). The most likely reason for this discrepancy at 300 °C is the difference in grain structure between the base alloy and Sc/Zr-containing alloys. Fig. 9a and b show the grain structures of alloys B and B15 after hot rolling, prior to tensile testing. The deformed grains were partially recrystallized in both alloys, presenting a mixture of recrystallized grains along the grain boundaries and elongated deformed grains in the rolling direction. In alloy B, the recrystallized grains were coarse, with an average size of 25 µm, and were randomly grown in the deformed grains. However, in alloy B15, there were often chains of tiny recrystallized grains with an average size of 8.4 µm along the grain boundaries.

At relatively low temperatures (25–200 °C), the fine recrystallized grains in the Sc/Zr-containing alloys can provide additional strengthening by retarding dislocation motion and grain rotation. In general, the difference in recrystallized grain size and distribution may not significantly affect the tensile strength. Therefore, the predicted ambient-temperature YSs matched well with the measured values for all three alloys.

However, at high temperatures (300 °C and up with sufficient thermal activation energy), the large numbers of fine recrystallized grains in the Sc/Zr-containing alloys, which covered large areas of the grain boundaries, became a major softening source by 1) acting as a vast channel for dislocation movement and vacancy diffusion [47, 48], and 2) facilitating localized deformation along the grain boundaries during tensile deformation. Grain boundary sliding has been reported as an operative deformation mechanism for fine-grained aluminum alloys at elevated temperatures and low strain rates [49, 50]. Griffiths *et al.* [51] reported that grain boundary sliding due to fine equiaxed grains in heat-treated Al–2.9 wt.% Mg–2.1 wt.% Zr alloy results in a significant drop in the YS at temperatures above 150 °C compared to that of the as-fabricated condition which comprises coarse columnar grains, although the ambient-temperature YS of the heat-treated alloy was always higher than that of the as-fabricated alloy. Therefore, it is reasonable to believe that the existence of many tiny recrystallized grains along the grain boundaries could reduce the YS at 300 °C to a large extent compared with the coarse recrystallized grain structure of alloy B owing to grain boundary sliding.

Fig. 9c and d show the grain structures of alloys B and B15, respectively, after tensile testing at 300 °C. Dynamic recrystallization continued heavily in alloy B during the tensile test at 300 °C, resulting in an increased recrystallization volume with coarse quasi-equiaxed grains. In this case, grain boundary sliding would be relatively weak. Therefore, the predicted and experimental YSs at 300 °C for alloy B were in good agreement (Fig. 8b). However, in alloy B15, a large number of tiny recrystallized grains still existed along the grain boundaries and even worsened during the tensile test owing to the restricting effect of $Al_3(Sc,Zr)$ precipitates on the coarsening of recrystallized grains. Consequently, grain boundary sliding would be activated and become much more pronounced than that in base alloy B. This explains the large reduction in YS of the Sc/Zr-containing alloys at 300 °C and the unexpected discrepancy between the predicted and

17

experimental values (Fig. 8b). However, it seems that the grain boundary sliding had a much less impact on the elevated-temperature UTSs, as the UTSs at 300–400 °C of all three alloys were very close (Figs. 5 and 6b).
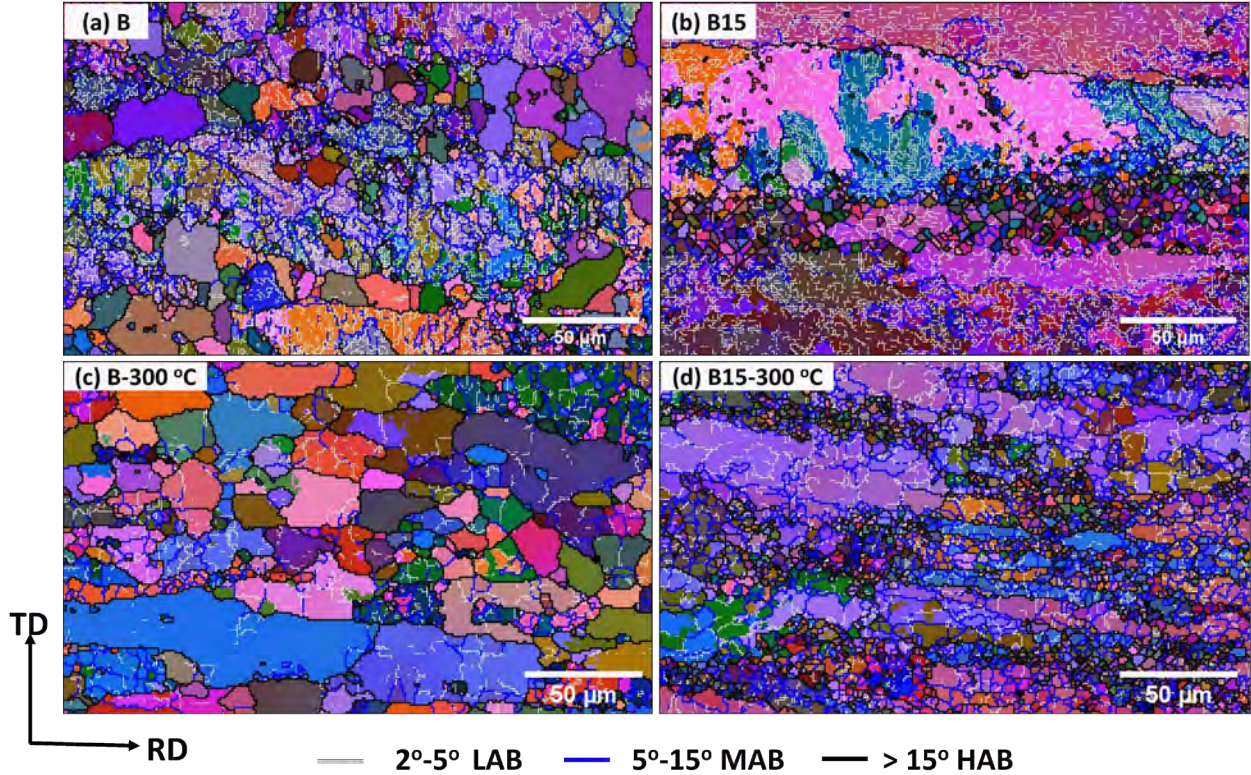

Figure 9: All Euler orientation maps, (a) alloy B and (b) alloy B15 samples after hot rolling prior tensile testing; (c) alloy B and (d) alloy B15 samples after tensile testing at 300 ºC.

4.3 Thermal stability of hot-rolled sheets and potential applications at high temperature

Table 5 presents a comparison of the elevated-temperature YSs and thermal stability of several commercial wrought aluminum alloys. The mechanical properties of most precipitation-strengthened Al alloys, such as 2xxx, 6xxx, and 7xxx alloys, deteriorate dramatically after thermal exposure at high temperatures, mainly because of rapid coarsening of the strengthening precipitates. The Al–Mg–Mn AA5083 alloys are potential candidates for high-temperature applications because its main strengthening mechanism (i.e., Mg solid-solution strengthening) is not prone to fade at high temperatures; the YS of conventional 5083 alloy at 315 °C is 52 MPa, which is much better than those of most precipitation-strengthened alloys [45]. More importantly, through the three-step heat treatment in the present work, a large number of thermally stable AlMn dispersoids were introduced into the aluminum matrix of the base alloy (Fig. 2a), which reinforced not only the ambient-temperature strength, but also the high-temperature strength (Figs. 4 and 5). The elevated-temperature YS (300 °C) reached 88 MPa in the hot-rolled sheets, resulting in an improvement of 70% relative to that of conventional AA5083 alloy. In particular, the YSs at 25 and 300 °C remained stable after long-term thermal exposure for up to 500 h because of the

18

superior thermal stability of the AlMn dispersoids (Fig. 7), making this hot-rolled alloy an excellent candidate as an engineering material for various elevated-temperature applications.

The present work focused on low-Sc alloys (Sc range of 0.08–0.15 wt.%) due to cost considerations. The AlMn dispersoids and $Al_3(Sc,Zr)$ precipitates are both thermally stable at elevated temperatures, and could synergistically improve the alloy strength. In addition, the precipitation temperature ranges of AlMn dispersoids and $Al_3(Sc,Zr)$ precipitates are similar and compatible (375–425 °C), which provides a common base for developing aluminum alloys with good high-temperature strength. However, this synergetic strengthening effect is limited to relatively low temperatures. At 20 - 200 °C, the addition of Sc and Zr significantly improves the tensile properties (Fig. 4). At higher temperatures (300–400 °C), the YSs of both Sc/Zr-containing alloys were lower than that of the base alloy (Fig. 6), restricting the application of Sc/Zr-containing alloys at high temperatures to some extent.

Owing to the poor rolling performance and the occurrence of alligator and crack defects during rolling [7], hot rolling was carried out at 500 °C in the present work, which caused extensive coarsening of the AlMn dispersoids and $Al_3(Sc,Zr)$ precipitates (Fig. 3). If the rolling performance can be improved and the rolling temperature lowered to 400–425 °C to reduce the coarsening of both types of particle, a better synergetic strengthening effect of the two types of particles and, hence, higher strength at high temperatures can be expected.

Table 5: Comparison of the YS at 300 ºC (MPa) of serval commercial wrought aluminum alloys

Alloys	YS at 300-315 ºC for various holding time					Reference
	0.5 h	10 h	100 h	500 h	1000 h	
2024-T6*	95	70	55	--	41	[45]
5083-O*	52	52	52		52	[45]
6061-T6*	75	55	31	--	29	[45]
7075-T6*	55	52	48	--	45	[45]
Alloy B (5083 base)	88	88	86	85	--	Present work
Alloy B08 (5083-0.08Sc)	66	66	67	69	--	Present work
Alloy B08 (5083-0.15Sc)	67	66	67	68	--	Present work

Note: * Test temperature and thermal exposure temperature was 315 ºC [45].

5.1 Conclusions

The effects of Sc and Zr additions to Al–Mg–Mn AA5083 alloys, particularly in the low Sc and Zr range (0.08–0.15 wt.%), on the microstructure and ambient/elevated-temperature mechanical properties were investigated. The results are summarized as follows:

1. The grain size of the as-cast microstructure was moderately decreased by the addition of Sc and Zr, whereas the area fraction of Fe/Mn-rich intermetallics and primary Mg_2Si remarkably increased.
2. Two populations of strengthening particles (AlMn dispersoids and Al_3(Sc,Zr) precipitates) precipitated in the Sc/Zr-containing alloys during the three-step heat treatment. However, the addition of Sc and Zr caused a reduction in AlMn dispersoids and an increase in dispersoid- free zones.
3. During hot rolling at 500 °C, both the AlMn dispersoids and Al_3(Sc,Zr) precipitates coarsened. The number density of AlMn dispersoids decreased by 60–80% after hot rolling, while the number density of Al_3(Sc,Zr) precipitates reduced by 71–76% compared to that in the heat-treated alloy (before rolling).
4. The tensile properties of the rolled sheets at 25–200 °C were significantly improved with increasing Sc and Zr content. The ambient-temperature YS and UTS of alloy B15 (with 0.16% Sc and 0.17% Zr) were 295 and 411 MPa, respectively, showing an improvement of 30% in YS and 11.8% in UTS compared to the base alloy. However, the YSs of the Sc/Zr-containing alloys at high temperatures (300–400 °C) were lower than those of the base alloy, most likely due to the grain boundary sliding mechanism.
5. The mechanical properties of the base and Sc/Zr-containing alloys were thermally stable during long-term thermal exposure at 300 °C for 500 h because of the superior thermal stability of the AlMn dispersoids and Al_3(Sc,Zr) precipitates, providing great potential for various high-temperature applications.
6. Constitutive analysis was applied to predict the YS contributions of the different strengthening mechanisms at 25 and 300 °C. The predicted YSs at 25 °C were in good agreement with the experimentally measured values. However, the predicted YSs at 300 °C of the Sc/Zr-containing alloys were quite different from the experimental ones. This discrepancy was predominantly due to the softening effect of grain boundary sliding, based on the EBSD results.

References

[1] J.R. Davis, Aluminum and Aluminum Alloys, Light Metals and alloys, (2001) 66-66.

[2] J.A.V.D. Hoeven, L. Zhuang, A New 5xxx Series Alloy Developed for Automotive Applications, SAE TECHNICAL PAPER SERIES, (2002) 1-8.

[3] E.L. Huskins, B. Cao, K.T. Ramesh, Strengthening mechanisms in an Al-Mg alloy, Materials Science and Engineering A, 527 (2010) 1292-1298.

[4] Ø. Ryen, B. Holmedal, O. Nijs, E. Nes, E. Sjölander, H.-E. Ekström, Strengthening mechanisms in solid solution aluminum alloys, Metallurgical and Materials Transactions A, 37 (2006) 1999-2006.

[5] Y. Li, A. Muggerud, A. Olsen, T. Furu, Precipitation of partially coherent α-Al (Mn, Fe) Si dispersoids and their strengthening effect in AA 3003 alloy, Acta Materialia, 60 (2012) 1004-1014.

[6] Z. Li, Z. Zhang, X.-G. Chen, Microstructure, elevated-temperature mechanical properties and creep resistance of dispersoid-strengthened Al-Mn-Mg 3xxx alloys with varying Mg and Si contents, Materials Science and Engineering A, 708 (2017) 383-394.

[7] K. Liu, X.G. Chen, Development of Al-Mn-Mg 3004 alloy for applications at elevated temperature via dispersoid strengthening, Materials & Design, 84 (2015) 340-350.

[8] A.M.F. Muggerud, E.A. Mørtsell, Y. Li, R. Holmestad, Dispersoid strengthening in AA3xxx alloys with varying Mn and Si content during annealing at low temperatures, Materials Science and Engineering A, 567 (2013) 21-28.

[9] K. Liu, H. Ma, X.G. Chen, Improving the elevated-temperature properties by two-step heat treatments in al-mn-mg 3004 alloys, Metallurgical and Materials Transactions B, 49 (2018) 1588-1596.

[10] A.Y. Algendy, K. Liu, X.G. Chen, Evolution of dispersoids during multistep heat treatments and their effect on rolling performance in an Al-5 % Mg-0 . 8 % Mn alloy, Materials Characterization, 181 (2021) 111487-111487.

[11] Z. Li, Z. Zhang, X.G. Chen, Improvement in the mechanical properties and creep resistance of Al-Mn-Mg 3004 alloy with Sc and Zr addition, Materials Science and Engineering A, 729 (2018) 196-207.

[12] E.A. Marquis, D.N. Seidman, Nanoscale structural evolution of Al 3 Sc precipitates in Al(Sc) alloys, Acta Materialia, 49 (2001) 1909-1919.

[13] D.N. Seidman, E.A. Marquis, D.C. Dunand, Precipitation strengthening at ambient and elevated temperatures of heat-treatable Al (Sc) alloys, Acta Materialia, 50 (2002) 4021-4035.

[14] P. Xu, F. Jiang, M. Tong, Z. Tang, J. Jiang, N. Yan, Y. Peng, Precipitation characteristics and morphological transitions of Al3Sc precipitates, Journal of Alloys and Compounds, 790 (2019) 509-516.

[15] E.A. Marquis, D.N. Seidman, Coarsening Kinetics of Nanoscale Al-3Sc Precipitates in an Al-Mg-Sc Alloy, Acta Mater., 53 (2005) 4259-4268.

[16] P. Xu, F. Jiang, Z. Tang, N. Yan, J. Jiang, X. Xu, Y. Peng, Coarsening of Al3Sc precipitates in Al-Mg-Sc alloys, Journal of Alloys and Compounds, 781 (2019) 209-215.

[17] C. Booth-Morrison, D.C. Dunand, D.N. Seidman, Coarsening resistance at 400 °c of precipitation-strengthened Al-Zr-Sc-Er alloys, Acta Materialia, 59 (2011) 7029-7042.

[18] C.B. Fuller, J.L. Murray, D.N. Seidman, Temporal evolution of the nanostructure of Al(Sc ,Zr) alloys:Part I -Chemical compositions of Al3(Sc1-xZrx) precipitates, Acta Materialia, 53 (2005) 5401-5413.

[19] C.B. Fuller, D.N. Seidman, D.C. Dunand, Mechanical properties of Al (Sc, Zr) alloys at ambient and elevated temperatures, Acta materialia, 51 (2003) 4803-4814.

[20] J. Lai, Z. Zhang, X.G. Chen, The thermal stability of mechanical properties of Al-B4C composites alloyed with Sc and Zr at elevated temperatures, Materials Science and Engineering A, 532 (2012) 462-470.

[21] P. Cavaliere, M. Cabibbo, Effect of Sc and Zr additions on the microstructure and fatigue properties of AA6106 produced by equal-channel-angular-pressing, Materials Characterization, 59 (2008) 197-203.

[22] T. Dorin, M. Ramajayam, J. Lamb, T. Langan, Effect of Sc and Zr additions on the microstructure/strength of Al-Cu binary alloys, Materials Science and Engineering A, 707 (2017) 58-64.

[23] G. Li, N. Zhao, T. Liu, J. Li, C. He, C. Shi, E. Liu, J. Sha, Effect of Sc/Zr ratio on the microstructure and mechanical properties of new type of Al-Zn-Mg-Sc-Zr alloys, Materials Science and Engineering A, 617 (2014) 219-227.

[24] G.B. Teng, C.Y. Liu, Z.Y. Ma, W.B. Zhou, L.L. Wei, Y. Chen, J. Li, Y.F. Mo, Effects of minor Sc addition on the microstructure and mechanical properties of 7055 Al alloy during aging, Materials Science and Engineering A, 713 (2018) 61-66.

[25] C. Xu, W. Xiao, R. Zheng, S. Hanada, H. Yamagata, C. Ma, The synergic effects of Sc and Zr on the microstructure and mechanical properties of Al–Si–Mg alloy, Materials & Design, 88 (2015) 485-492.

[26] M. Li, Q. Pan, Y. Shi, X. Sun, H. Xiang, High strain rate superplasticity in an Al–Mg–Sc–Zr alloy processed via simple rolling, Materials Science and Engineering A, 687 (2017) 298-305.

[27] F. Liu, Z. Ma, Achieving exceptionally high superplasticity at high strain rates in a micrograined Al–Mg–Sc alloy produced by friction stir processing, Scripta Materialia, 59 (2008) 882-885.

[28] Y. Luo, Q. Pan, Y. Sun, S. Liu, Y. Sun, L. Long, X. Li, X. Wang, M. Li, Hardening behavior of Al-0.25 Sc and Al-0.25 Sc-0.12 Zr alloys during isothermal annealing, Journal of Alloys and Compounds, 818 (2020) 152922.

[29] D. Pan, S. Zhou, Z. Zhang, M. Li, Y. Wu, Effects of Sc(Zr) on the microstructure and mechanical properties of as-cast Al–Mg alloys, Materials Science and Technology (United Kingdom), 33 (2017) 751-757.

[30] S.A. Zhou, Z. Zhang, M. Li, D. Pan, H. Su, X. Du, P. Li, Y. Wu, Effect of Sc on microstructure and mechanical properties of as-cast Al-Mg alloys, Materials & Design, 90 (2016) 1077-1084.

[31] L.L. Rokhlin, N.R. Bochvar, I.E. Tarytina, N.P. Leonova, Phase composition and recrystallization of Al-based Al-Sc-Mn-Zr alloys, Russian Metallurgy (Metally), 2010 (2010) 241-247.

[32] E.M. Elgallad, K. Liu, Z. Zhang, X.G. Chen, Effect of transition elements on dispersoid formation and elevated-temperature mechanical properties in 6082 aluminum alloy, Philosophical Magazine, 101 (2021) 96-116.

[33] K. Liu, E. Elgallad, C. Li, X.G. Chen, Effects of Zr and Sc additions on precipitation of α-Al(FeMn)Si dispersoids under various heat treatments in Al-Mg-Si AA6082 alloys, International Journal of Materials Research, 112 (2021) 706-716.

[34] E.A. Marquis, D.N. Seidman, M. Asta, C. Woodward, Composition evolution of nanoscale Al3Sc precipitates in an Al-Mg-Sc alloy: Experiments and computations, Acta Materialia, 54 (2006) 119-130.

[35] Z. Li, Z. Zhang, X.G. Chen, Effect of Metastable Mg2Si and Dislocations on α-Al(MnFe)Si Dispersoid Formation in Al-Mn-Mg 3xxx Alloys, Metallurgical and Materials Transactions A, 49 (2018) 5799-5814.

[36] K. Liu, H. Ma, X.G. Chen, Improving the Elevated-Temperature Properties by Two-Step Heat Treatments in Al-Mn-Mg 3004 Alloys, Metallurgical and Materials Transactions B, 49 (2018) 1588-1596.

[37] M.J. Starink, N. Gao, N. Kamp, S.C. Wang, P.D. Pitcher, I. Sinclair, Relations between microstructure, precipitation, age-formability and damage tolerance of Al-Cu-Mg-Li (Mn, Zr, Sc) alloys for age forming, Materials Science and Engineering A, 418 (2006) 241-249.

[38] W. Lefebvre, F. Danoix, H. Hallem, B. Forbord, A. Bostel, K. Marthinsen, Precipitation kinetic of Al3(Sc, Zr) dispersoids in aluminium, Journal of Alloys and Compounds, 470 (2009) 107-110.

[39] M. Cabibbo, E. Evangelista, M. Vedani, Influence of severe plastic deformations on secondary phase precipitation in a 6082 Al-Mg-Si alloy, Metallurgical and Materials Transactions A, 36 (2005) 1353-1364.

[40] I. Lomaev, E. Elsukov, On the analysis of the mechanisms of the strain-induced dissolution of phases in metals, Physics of Metals and Metallography C/C of Fizika Metallov I Metallovedenie, 102 (2006) 186.

[41] J. Rakhmonov, K. Liu, P. Rometsch, N. Parson, X.G. Chen, Effects of Al(MnFe)Si dispersoids with different sizes and number densities on microstructure and ambient/elevated-temperature mechanical properties of extruded Al–Mg–Si AA6082 alloys with varying Mn content, Journal of Alloys and Compounds, 861 (2021) 157937.

[42] K.L. Kendig, D.B. Miracle, Strengthening mechanisms of an Al-Mg-Sc-Zr alloy, Acta Materialia, 50 (2002) 4165-4175.

[43] L. Tang, X. Peng, J. Huang, A. Ma, Y. Deng, G. Xu, Microstructure and mechanical properties of severely deformed Al-Mg-Sc-Zr alloy and their evolution during annealing, Materials Science and Engineering A, 754 (2019) 295-308.

[44] J. Qin, Z. Zhang, X.G. Chen, Mechanical Properties and Strengthening Mechanisms of Al-15 Pct B4C Composites with Sc and Zr at Elevated Temperatures, Metallurgical and Materials Transactions A, 47 (2016) 4694-4708.

[45] J.G. Kaufman, Properties of aluminum alloys: tensile, creep, and fatigue data at high and low temperatures, ASM international, 1999.

[46] A.J. Ardell, Precipitation hardening, Metallurgical Transactions A, 16 (1985) 2131-2165.

[47] A.H. Chokshi, Grain boundary processes in strengthening, weakening, and superplasticity, Advanced Engineering Materials, 22 (2020) 1900748.

[48] X. Zhang, H. Wang, B. Yan, C. Zou, Z. Wei, The effect of grain refinement and precipitation strengthening induced by Sc or Er alloying on the mechanical properties of cast Al-Li-Cu-Mg alloys at elevated temperatures, Materials Science and Engineering A, 822 (2021) 141641.

[49] F. Musin, D.R. Lesuer, T.G. Nieh, Superplastic behavior of an Al - Mg alloy at elevated temperatures, Material Science and Engineering A, 342 (2003) 169-177.

[50] A. Venkataraman, M. Linne, S. Daly, M.D. Sangid, Criteria for the prevalence of grain boundary sliding as a deformation mechanism, Materialia, 8 (2019) 100499.

[51] S. Griffiths, J.R. Croteau, M.D. Rossell, R. Erni, A. De Luca, N.Q. Vo, D.C. Dunand, C. Leinenbach, Coarsening- and creep resistance of precipitation-strengthened Al–Mg–Zr alloys processed by selective laser melting, Acta Materialia, 188 (2020) 192-202.